

## Overbias and Quantum Tunneling in Light-Emitting Memristors


S. Hamdad,<sup>1</sup> K. Malchow<sup>1</sup>,<sup>1</sup> D. Avetisyan,<sup>1</sup> E. Dujardin<sup>1</sup>,<sup>1</sup> A. Bouhelier<sup>1</sup>,<sup>1,\*</sup> Y. Zhou,<sup>2</sup> B. Cheng,<sup>2</sup> T. Zellweger<sup>3</sup>,<sup>3</sup> and J. Leuthold<sup>4</sup>

<sup>1</sup>*Laboratoire Interdisciplinaire Carnot de Bourgogne, CNRS UMR 6303 Université de Bourgogne Franche-Comté, Dijon 21000, France*

<sup>2</sup>*Microelectronics Thrust, Function Hub, Hong Kong University of Science & Technology, Guangzhou, China*

<sup>3</sup>*ETH Zurich, Integrated Systems Laboratory, Zurich 8092, Switzerland*

<sup>4</sup>*ETH Zurich, Institute of Electromagnetic Fields, Zurich 8092, Switzerland*

 (Received 6 December 2022; revised 25 May 2023; accepted 25 July 2023; published 23 August 2023)

A nanoscale dielectric gap clamped between two metal electrodes may undergo a large resistance change from insulating to highly conducting upon applying an electrical stress. This sudden resistive switching is largely exploited in memristors for emulating synapses in neuromorphic neural networks. Here, we show that volatile resistive switching can be accompanied by a release of electromagnetic radiation spanning the visible spectral region. Of note, we find that the spectrum is characterized by photon energies exceeding the maximum kinetic energy of electrons provided by the switching voltage. This so-called overbias emission can be described self-consistently by a thermal radiation model featuring an out-of-equilibrium electron distribution generated in the device with an effective temperature exceeding 2000 K. The emitted spectrum is understood in terms of hot electrons radiatively decaying to resonant optical modes occurring in a nanoscale SiO<sub>2</sub> matrix located between two Ag electrodes. We further show that the same device can sustain different emission mechanisms depending on the nature, the intricacy and historicity of its memristive gap. Specifically, when operated in a nonvolatile state, we identify inelastic electron tunneling as an additional process providing photon emission from the device. The correlation between resistive switching and the onset of light emission in atomic scale photonic memristor brings alternative venues to generate light on chip and their exploitation in optical interconnects. Photons emitted during memristive switching can also be monitored to follow the neural activation pathways in memristor-based networks.

DOI: [10.1103/PhysRevApplied.20.024057](https://doi.org/10.1103/PhysRevApplied.20.024057)

### I. INTRODUCTION

Despite its apparent simple geometry, a nanometer-wide gap separating two metal tips constitutes a unique interdisciplinary fertile ground for exploring electrical, optical, chemical, and biological interactions down to the molecular or even atomic scale. On one hand, extremely large static electric fields ( $>10^8$  Vm<sup>-1</sup>), intense electromagnetic enhancement reaching several orders of magnitude [1], and record-high nm<sup>3</sup> optical mode volumes [2] are now achievable with gap structures fabricated by modern patterning tools. These figures have enabled a variety of electronic and optical spectroscopies at the single molecule level [3,4] and have fostered the emergence of alternative research territories such as optics in picocavities [5], molecular optomechanics [6], quantum plasmonics [7,8], and trapping at the nanoscale [9,10] to name a few.

On the other hand, electronic components integrating a nanometer-scale gap in their design were also crucial

to the advent of another form of computing. Memristors, for instance, are programmable voltage-dependant resistive devices deployed nowadays in cognitive hardware systems such as artificial neural networks, neuromorphic and reservoir computing [11,12]. In these devices, memory and processing are co-located on the same component enabling thus lower-energy consumption, higher speeds, and scalability [13]. Memristive operation relies on resistance switching triggered by the electroformation and disruption of conductive pathways within a nanometer-scale dielectric gap [14]. Depending on the metal and the nature of the insulating layer, charge transport occurs by an electrochemical reduction of metal ions aggregating to form conductive filaments [14], or by migration of mobile defects, such as oxygen vacancies [15] and nanoclusters [16,17]. It has been recognized that such voltage-triggered modifications of the dielectric gap not only affect charge transport in the device, but also opens alternative control strategies over optical functionalities as well [18–22].

A particular interesting functionality enabled by ultra-small gaps is the generation of light by inelastic electron

\*alexandre.bouhelier@u-bourgogne.fr

tunneling (IET). Such an electrically driven junction acts as a tunable optical antenna converting electrical energy into light that can be deployed for the next generation of on-chip integrated photon sources [23,24]. It is not clear, however, if such an effect can be observed when the tunneling dielectric changes its conduction properties. In switchable resistive gap, the dielectric layer evolves dynamically and the situation drastically differs from the passive tunneling barrier generally employed in electrically driven optical antennas. The correlation between electrical and emission properties is quite challenging and the time evolution of the memristive barrier becomes a critical characteristic. This is particularly the case for Ag/SiO<sub>2</sub>/Ag configuration because the conductance of the device undergoes different transport regimes with the growth of a filament in the dielectric. For instance, defect-induced electroluminescence has been observed during the electroformation of a planar Ag/SiO<sub>2</sub>/Pt memristor [25]. A complete electrochemical formation of the filament changes the nature of transport when the conductance of the device  $G$  increases close to the quantum point contact  $G_0 = 2e^2/h = 7.75 \times 10^{-5}$  S, where  $h$  is the Planck constant and  $e$  is the elementary charge. Near this conductance value even a small atomic reorganization of the gap induces a significant variation of the conductance. Indeed, electrons injected and transported through the gap may take different pathways (tunneling, hopping, ballistic, etc. [15]), which are all determined by the dielectric properties of the gap and the bias value. This aspect sets the significance of a precise and accurate control of the applied electrical constraint as it defines the irreversible historicity of the memristive junction.

In this paper we identify two distinct light-emission mechanisms occurring in a memristive Ag/SiO<sub>2</sub>/Ag junction that are departing from defect luminescence. Specifically, we show that when the device undergoes resistive switching to a conductance value slightly below  $G_0$  light may be released either in the so-called overbias emission regime or by inelastic electron tunneling. These two modes of emission can be distinguished by their dependencies on the electrical conditions and their spectra. In overbias emission, the energy  $h\nu$  of the photons emitted exceeds the kinetic energy  $eV_b$  of a single electron traversing the device.  $\nu$  is the frequency of light and  $V_b$  is the voltage drop at the two terminals of the device. For IET, the condition  $h\nu < eV$  applies. Overbias emission has been repeatedly observed in various types of metal contacts ranging from discontinuous islands [26], electromigrated nanowires [27,28], mechanical break junctions [29], and scanning tunneling experiments [30,31], but has not been associated to the memristive change of a dielectric matrix. A memristor has several key advantages compared to other geometries. The device holds a dual functionality whereby electrons and photons are controlled by the same atomic scale system, its response

can be cycled and it offers potential for integration and scalability.

## II. FABRICATION AND ELECTROFORMATION OF THE DEVICE

The device geometry discussed here is constituted of two in-plane 70-nm-thick silver electrodes thermally deposited on an ultrathin Cr adhesion layer (approximately 1 nm) on top of a SiO<sub>2</sub> glass coverslip. The electrodes are terminated by a tapered section forming a 90° angle and are separated by a gap of about 60 nm. The structure is realized by electron-beam lithography complemented by metal deposition and a liftoff process. The inset of Fig. 1(a) shows a SEM of a nominal device.

The device is operated under ambient conditions and its electro-optical responses are measured using the setup schematically presented in Fig. 1(a). The junction is electrically driven by a voltage source applied on one electrode while the other is connected to a transimpedance amplifier (TIA). The TIA accurately measures the current flowing in the device. During the initial characterization steps described below, we introduce protection resistors to limit the maximum current. Light emission produced by the device is collected by a high numerical aperture objective and is directed to an avalanche photodiode for recording the photon count rate and to an imaging spectrometer for analyzing the spectral content.

For a 60-nm gap size and biases of a few volts, the dielectric spacer is too large to enable electrons to tunnel from one electrode to the other; the device is in a high resistive state (HRS). To initiate memristive switching to a low resistive state (LRS), we repeatedly stress the device by applying voltages of increasing amplitudes until a current is detected. We add a resistor in series to control the compliance current in the nanojunction and to prevent overheating of the device. We use different resistors from 100 MΩ when the device is at the highest resistance state to 10 kΩ, which is the targeted low resistive state (approaching  $R_0 = G_0^{-1}$ ). The activation procedure requires to lower the protection resistor (increasing compliance current) whenever the current approaches and stabilizes near its compliance value. This enables to slowly build the conductive path in the dielectric and to minimize the electrical failure. During this electroformation phase, a conduction path dominantly composed of a mixture of silver aggregates builds up between the electrodes [32,33] and a low current (approximately nA) flowing can be registered. This step is critical as it constitutes the historicity of the junction, the morphology of the conduction path and the electrical characteristics at which the device will operate. Figure 1(b) is a time trace of the normalized conductance of the device  $G/G_0$  recorded during the last electroformation stress. The conductance, estimated by taking into account a constant driving voltage (400 mV)

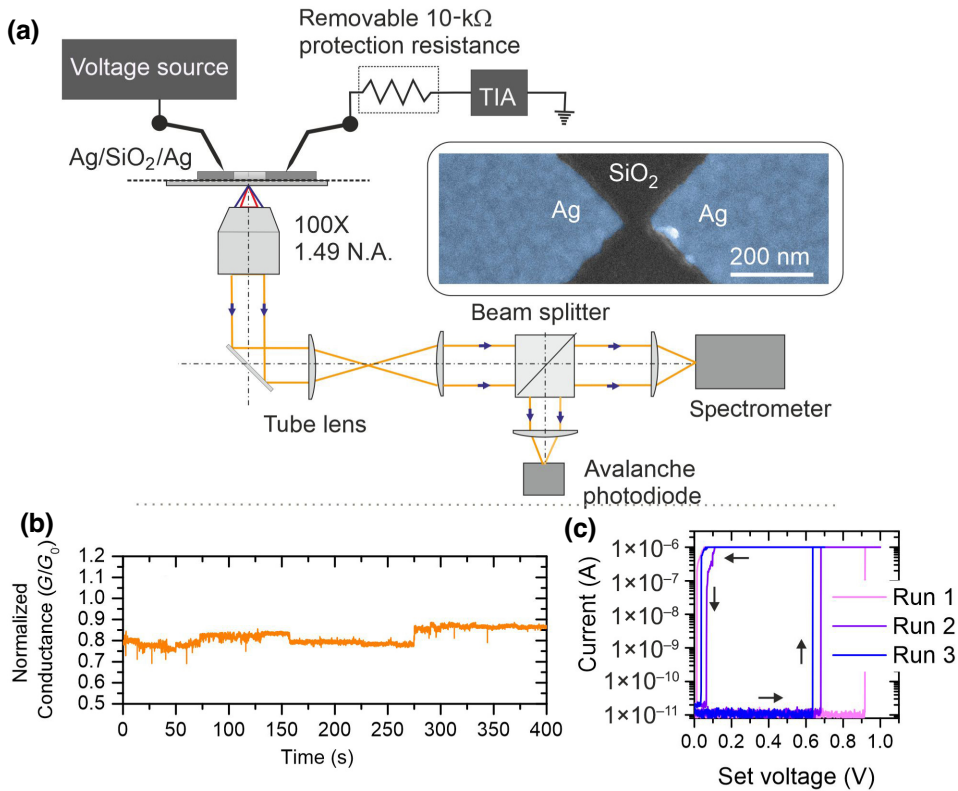


FIG. 1. (a) Schematic representation of the experiments including the electrical excitation and signal recovery with transimpedance amplifier (TIA) as well as the optical detection. Inset: SEM image of a typical in-plane Ag/SiO<sub>2</sub>/Ag junction. Ag is colorized with a blue hue and a sacrificial conducting layer has been deposited to allow for electron imaging. (b) Time trace of the device's normalized conductance  $G/G_0$  during the final stage of the activation process. (c) Current-to-voltage characteristics for three consecutive voltage sweeps showing resistive switching.

and the voltage drop at the protection resistance, is here stabilized slightly below  $G_0$ . This suggests that current transport is taking place through an imperfect filament formation and not fully opened channel. The steplike evolution of  $G/G_0$  observed at different moments (e.g.  $t = 72$  s, 155 s, or 275 s) indicates a dynamic reorganization of the current pathways either by a migration of species or ionization of charge traps. This conductance closed to  $G_0$  is unstable and relaxes to a HRS when the electrical stress is stopped. This is an asset in our study because we intend to capture the emission property of a volatile memristive device repeatedly switching to conductance values near  $G_0$ . Once the junction is electroformed, reversible resistive switching from HRS to LRS occurs when the first filamentary conductive path connects these discontinuous nanoclusters. Figure 1(c) shows the expected switching behavior for three consecutive voltage sweeps of a typical activated device. The characteristics are acquired here with a semiconductor analyzer with a compliance current set at 1  $\mu$ A.

### III. ELECTRO-OPTICAL PROPERTIES OF THE DEVICE

The dynamic of filament formation and the resulting conductance are typically triggered by two crucial parameters, which are the applied voltage and the growth time. To avoid the formation a complete silver bridge, which would be materialized by a diffusive transport regime ( $G \gg G_0$ )

and no photon emission, we operate the electroformed device with sequences of 1.24-V voltage pulses. Each sequence is composed of 100 pulses with 100-ms duration and a period of 500 ms. The rising edge of the pulse is 1.3  $\mu$ s. At the beginning of the sequence, the volatile nature of the memristive conductive path helps the system to relax (LRS  $\Rightarrow$  HRS) during the time the voltage is off, thus preventing a metallic contact to form between the two electrodes. Joule heating during transport may also contribute to destabilize the filament and prevent the complete growth because the protection resistance has been removed after the electroformation phase of the device in order to have all the applied voltage dropped at the gap.

Figure 2(a) shows a typical behavior of the current acquired during an approximately 1-mn-long pulse sequence. During the first 12 s, the device remains in a HRS and the current is at the noise floor, here about 400 nA. From 12 s  $< t < 20.7$  s, a small current (approximately 1.5  $\mu$ A) indicates a progressive build up of the conduction paths. Resistive switching depends of the number of available Ag ions present in the dielectric layer. At the beginning of the sequence, too few ions are present to switch the device. At  $t > 21$  s, the device undergoes a clear resistive switching to a LRS at each voltage pulse. We observe a transient response with the occurrence of fluctuating current peaks up to  $t \sim 32$  s. The LRS current then stabilizes to about 8.5  $\mu$ A during the rest of the sequence. During this stable phase, the current is established at the onset of the voltage pulse. This suggests the formation

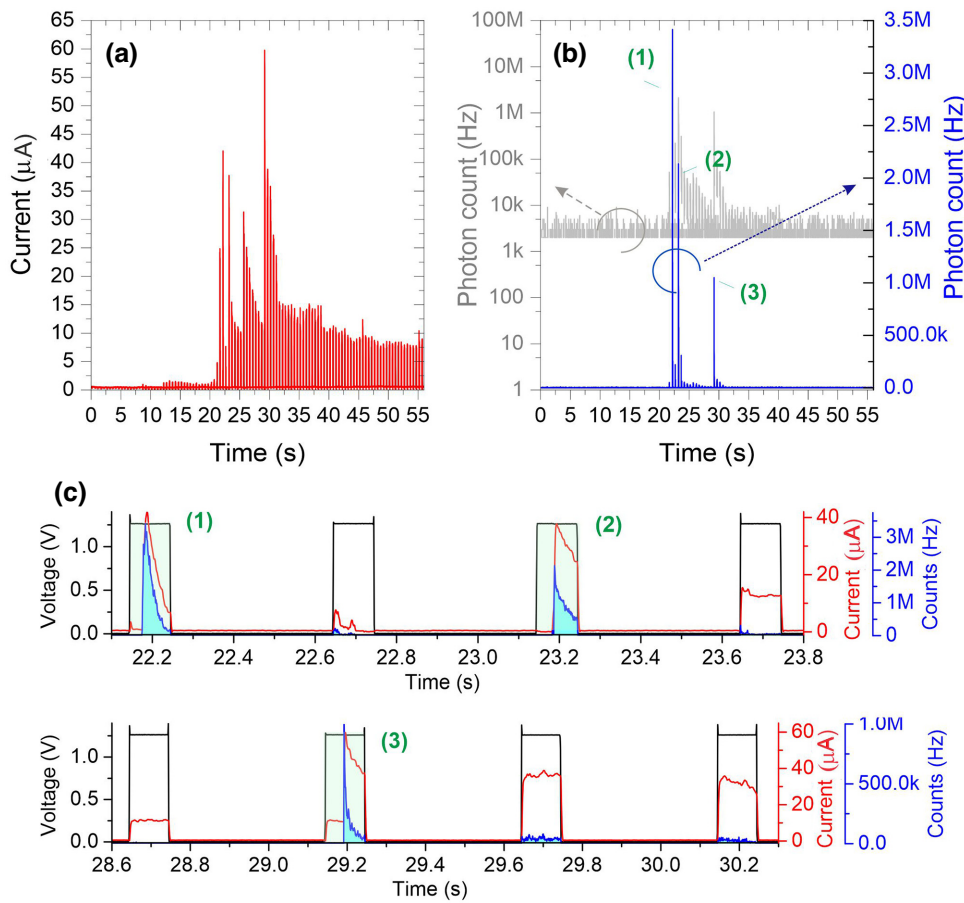


FIG. 2. (a),(b) Time trajectories of the current and photon counts acquired during the application of a train of voltage pulses ( $V_b = 1.24$  V, not shown for the sake of clarity). Photon counts are represented on linear (blue) and logarithmic (gray) scales. (c) Temporal sequence featuring the three most intense events (shaded pulses) labeled (1), (2), and (3) in (b).

a stable conduction channel with retention time greater than the pulse period [34]. In this nonvolatile regime of operation and at that voltage bias, no light is detected.

However, during the transient phase ( $20 < t < 32$  s) the APD records a strong optical activity. This is clearly depicted in Fig. 2(b) showing the time trace of the photon counts. To appreciate even the dimmest light emission, we also plot the count rate in logarithmic units (gray curve, right axis). The photon count is particularly large for three switching pulses at  $t = 22.18$  s,  $t = 23.18$  s, and  $t = 29.29$  s, labeled (1), (2), and (3), respectively. There, the count rates are in excess of 1 MHz, a value nearly 2 orders of magnitude higher than typical single-molecule rates (kHz) detected within the same diffraction-limited volume [35]. Figure 2(c) shows a time extract of the transient phase where most of the photons are detected. The intense events are highlighted by shaded areas and are occurring at peaking conductance values of  $G \sim 0.4G_0$ ,  $G \sim 0.35G_0$ , and  $G \sim 0.6G_0$ , respectively. Note that both current and photon counts have a delayed response of approximately 30 ms with respect to the rising edge of the voltage pulse. The delay is understood from the intrinsic dynamics of the memristive conductive path formation and similar switching time has been reported in the literature [36]. The kinetics strongly depends on the nature of the device (material,

structure, etc.) and the density of ions available [34]. It can vary easily by an order of magnitude. Our device geometry is not optimized for a fast switching as we operate large gaps (ca. 60 nm) with a rather low voltage (1.24 V).

In contrast, a stable and somewhat lower LRS (i.e., a weakly fluctuating current during the pulse) triggers little or no optical activity from the device. During these pulses, the onset of the electron flow is concurrent to the rising edge of the voltage pulse (no delayed response) indicating that the preceding pulse induced the formation of a non-volatile low-resistance state [34]. This is seen, for instance, in Fig. 2(c) for the optically dark cycles at  $t = 23.65$  s and  $t = 28.65$  s.

Focusing the discussion on the volatile transients, we observe an obvious correlation between the luminous events and the current peaks linked to the unsteady LRS. This is seen within the shaded pulses of the time traces in Fig. 2(c) where a rapid drop of the current is observed after the emission is triggered. Photons are clearly produced during a dynamic reconfiguration of the current path within the device. A detailed explanation of the current fluctuations is still unclear. A series of mechanisms may contribute to the effect including atomic reshaping of the filament and suppression of conduction channels by charged traps.

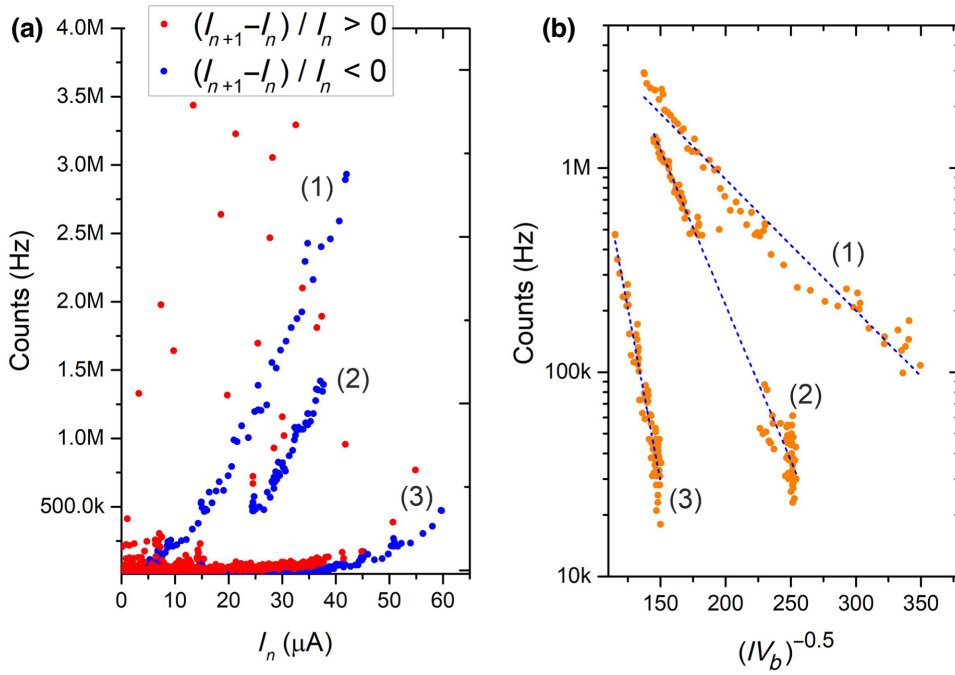


FIG. 3. (a) Separate contributions of the relative increase (red circles) and the relative decrease of the current (blue points) to the photon count rate. The three branches forming the blue data set are linked to events (1) to (3) of Fig. 2. (b) Logarithmic plot of the count rate as a function of the inverse square root of the dissipated power for each of the three branches observed in (a).

To investigate the correlation between current fluctuations and photon generation, we examine their dependence by analyzing the variation  $\Delta I = I_{(n+1)} - I_n$  inferred around each  $I_n$  values, where  $n$  is the current bin number in the time trace. Results are shown in Fig. 3(a). The plot separates the contribution to the light emission of a relative increase of the current ( $\Delta I/I > 0$ ) to that of a relative decrease of the current ( $\Delta I/I < 0$ ). For positive variation leading to an increase of the current, the device generally has a very low optical activity (red circles). There are a few scattered points associated with the detection of intense signal but there is no clear trend with the current. We conclude that the photon count is not related to the number of electrons flowing in the device for  $\Delta I/I > 0$ . In contrast, for negative fluctuations of the current, three branches clearly appear in the graph (blue circles). These branches are related to the sequence of the three most luminous events observed on the time trace of Fig. 2. A series of observations can be made by analyzing Fig. 3(a). First, the correlation plot reveals the nonlinear nature of the photon signal since the emission is only detected after a current threshold. The onset of current triggering photon emission increases with each branch with  $I \sim 3 \mu\text{A}$  for (1),  $I \sim 10 \mu\text{A}$  for (2) and  $I \sim 35 \mu\text{A}$  for (3) implying an evolutionary response. Second, Fig. 3(a) also shows that the absolute amplitude of the current is not the proper parameter that sets the rate at which the device emits: a similar current gives different photon counts for the three branches. These two observations taken together suggest an underlying sensibility of the emission to the peculiarity of the current channel formation at the atomic level as well as the history of the device. Third, the correlation

between photon counts and negative  $\Delta I/I$  clearly indicates that the process of light emission affects the electron transport within the device. We shall come back to this point later in the discussion.

#### IV. OVERBIAS EMISSION

Let us discuss now the origin of the light signal. Our starting point is the following: the avalanche photodiode used in the experiment has a detection efficiency peaking at 1.77 eV (700 nm), which rapidly vanishes to  $<2\%$  below 1.2 eV. Any emission mechanism promoted by a single electron process would therefore be emitted in the nearly blind spectral region of the detector. The optical activity registered in the time traces of Fig. 2 suggests that the memristive device releases all of the detected photons in an overbias emission regime. Opposite to single electron process producing photon energies smaller than the voltage applied ( $h\nu \leq eV_b$ ), overbias light emission (or sometimes referred as above-threshold or anomalous) requires the cumulative contributions of multiple electrons.

Different mechanisms have been proposed to explain overbias emission including thermal broadening of the Fermi-Dirac distribution [37], coherent multielectron scattering [38–42] and decay of hot carriers [27,29,43]. For interacting systems with characteristic dimensions smaller than the electron mean-free path (about 30 to 60 nm for noble metals at room temperature [44,45]) and high pumping conditions, the effective temperature of the electron subsystem  $T_e$  may be set by the electrical power dissipated. This is the main line of argumentation put forward by Fedorovich, Naumovets, and Tomchuk in their pioneer

work on electrically connected discontinuous island film [46], where the power dissipated in the system results to steady-state nonequilibrium electron and lattice temperatures ( $T_e \neq T_L$ ). Under this circumstance, the electron temperature is written  $T_e = \sqrt{\alpha IV_b}/k_B$  and can reach values greatly exceeding the lattice temperature, which remains virtually unchanged ( $T_e \gg T_L$ ). Here  $k_B$  is Boltzmann's constant and  $\alpha$  is an empirical factor, which depends on the exchange interaction between electrons and lattice phonons [27,43].

In this picture, the net energy gain observed for photon in the regime of overbias ( $h\nu \geq eV_b$ ) is attributed to inelastic scattering of the hot electrons with the physical boundaries giving rise to a bremsstrahlung emission [47]. However, thermal bremsstrahlung of colliding hot electrons cannot be distinguished from a spontaneous decay of out-of-equilibrium electrons because both mechanisms obey the same energy dependence in the detected energy range [47,48]. The problem can be reduced to a simple blackbody thermal radiation model [46] with spectral density  $U(V_b, \nu)$ .

$$U(V_b, \nu) \propto \rho(\nu) h\nu e^{-h\nu/\sqrt{\alpha IV_b}}, \quad (1)$$

where  $\rho(\nu)$  is the local density of optical states. Equation (1) can be reformulated to

$$\ln[U(V_b, \nu)] \propto \ln[\rho(\nu) h\nu] - \frac{h\nu}{\sqrt{\alpha IV_b}}. \quad (2)$$

Equation (2) highlights the expected dependence of the light signal with the electrical power  $IV_b$  dissipated in the device. Figure 3(b) shows the photon count rate in logarithmic scale as a function of the parameter  $1/\sqrt{IV_b}$  extracted from the three branches of Fig. 3(a). Clearly, the data associated to each  $i$  branch follow the expected linear dependence of the heated electron gas model [Eq. (2)] with slopes given by  $\beta_{(i)} = -h\nu/\sqrt{\alpha_{(i)}}$ . The dashed blue curves are linear fits to the data providing  $|\beta_{(1)}| = 15 \times 10^{-3} \text{ W}^{1/2}$ ,  $|\beta_{(2)}| = 35 \times 10^{-3} \text{ W}^{1/2}$  and  $|\beta_{(3)}| = 78 \times 10^{-3} \text{ W}^{1/2}$ . These slopes give only an estimate because the photon count integrates the light emitted over the whole detection energy. In the framework of a radiative decay of a nonequilibrium electron gas, the effective steady-state electron temperature is dependent on how fast heat can be transferred from the side walls of the structure and also depends on characteristic dimensions of the conduction channel [47]. Since the device undergoes a reorganization during volatile switching, the different  $\beta_{(i)}$  values are related to the particularity of the atomic geometry, which dictates the thermalization process of electrons. In any case, and with the present device's geometry, coupling to the radiation bath remains a very inefficient process. We have estimated the external quantum efficiency (QE) by integrating the count rate during pulses and dividing it by

the measured number of electrons traversing the device in the same time. For the brightest of the three events the QE is  $8 \times 10^{-9}$  photon per electron.

We confirm that our results are in line with this out-of-equilibrium regime by two conclusive observations. Assuming a photon energy at the peak efficiency of the detector, we can easily estimate an effective electronic temperature using the relation  $T_e = \sqrt{\alpha IV_b}/k_B$ . If we take, for instance, the second branch  $i = 2$ , we find that  $T_e$  is about 4000 K at the highest count rate and 2300 K at the lowest. This range of  $T_e$  is consistent with electronic temperatures reported in electromigrated junctions and quantum point contacts operated under comparable electrical excitation and emitting also in the overbias regime [27,43,47].

In our planar memristive junction, there is a clear interdependence between the current transported in the device and the light emission. During the pulses providing the brightest events displayed in the time trace of Fig. 2(c), current and photon counts share a similar decaying behavior. This correlative feature suggests that the thermalization process of hot carriers affects the transport, probably by gradually disrupting the filamentary pathway during the thermalization process. In turn, the electrical power dissipated in the system reduces, and  $T_e$  decreases concomitantly to its overbias electromagnetic signature. If photon release is not a desired property of the device, then the stability of LRS may be improved by increasing the concentration of metal ions. This will reduce the set voltage and lower the overbias probability.

The second experimental evidence confirming the origin of the light released upon resistive switching is its spectral content. Figure 4(a) shows the spectrum acquired during the second luminous event recorded in the time trace of Fig. 2(c). The spectrum is corrected for the overall collection efficiency of our instrument, shown in the dashed gray curve, using the objective and spectrometer's specifications. The correction explains the enhanced noise at low energies where the silicon detector has a vanishing efficiency. The corrected spectrum features a characteristic decay tail consistent with an overbias emission regime. The light recorded during the switching pulse clearly violates the quantum cutoff set by a single electron process ( $h\nu = eV_b$ ) because the maximum photon energy (approximately 2 eV) largely exceeds the kinetic energy of carriers (1.24 eV). The spectrum cannot be explained by any linear electroluminescent colored centers, which may be present within the dielectric matrix and emitting over a defined energy range [25] and is also very different from a coherent multielectron emission mechanism where clear spectral signatures appear at  $neV_b$  associated with  $n$ -electron processes [38,49].

The spectrum shows a series of shoulders, which under the light of Eq. (1), can be reasonably interpreted by the spectral evolution of the local density of optical states  $\rho(\nu)$ . Photon emission is here triggered by hot electrons

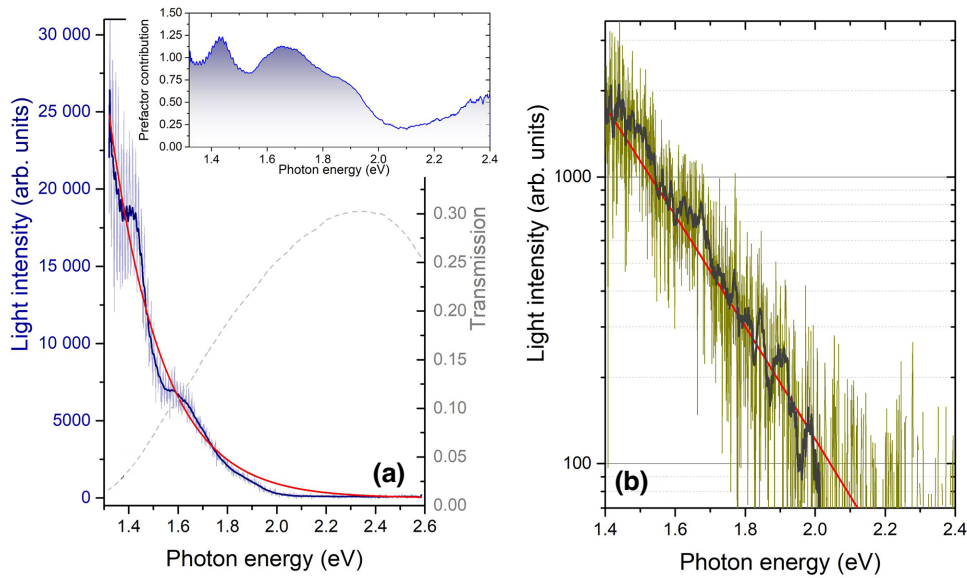


FIG. 4. (a) Overbias emission spectrum of the second luminescent event (2). The light blue line (left axis) is the corrected spectrum taking into account the spectral efficiency of the detection (gray curve, right axis). The dark blue line is an adjacent averaging. The red line is a fit of the data using Eq. (1) with a dispersionless prefactor  $\rho$ . Inset: spectral contribution of the prefactor obtained after normalizing the experimental spectrum by Planck's contribution. (b) Overbias emission spectrum of the third luminescent event (3) registered in Fig. 2(b). The red line is a fit of the data using Eq. (1) with a dispersionless prefactor  $\rho$  and  $T_e = 2300$  K. Semilogarithmic scale.

colliding with the boundaries of a complex optical environment sustaining a rich surface plasmon landscape. Various multipolar modes are existing and possibly hybridizing in such ill-defined gap morphology [50]. Energy dispersion of  $\rho(\nu)$  is thus expected in such composite nanoscale structures [27,28]. An independent confirmation of these resonances is a daunting task because the characteristic length at which the interaction occurs is beyond the capabilities of standard optical spectroscopies. Nonetheless, we tentatively extract from the spectrum an effective temperature of the electron bath giving rise to the overbias light emission. We fit the averaged data points [blue line in 4(a)] with Eq. (1) considering a constant prefactor  $\rho$  and replacing  $\sqrt{\alpha IV_b}$  by the standard temperature dependence  $k_B T_e$ , with  $T_e$  used as a free parameter. The fit is shown as the red line with  $T_e = 2127$  K. Deviation of the model from the data set is linked to the dispersion of prefactor  $\rho(\nu)$  discussed below.

Conservation of energy requires that  $k_B T_e \leq eV$ . Using the electron temperature extracted from the fit of Fig. 4(a), we find that  $k_B T_e / eV$  is about 0.14. The value is consistent with a previous report of overbias emission obtained with STM point contacts [30]. The inferred electron temperature is a little bit lower than the range of effective  $T_e$  inferred by analyzing Fig. 3 where  $2300 \text{ K} < T_e < 4000 \text{ K}$ . The discrepancy is probably linked to the accuracy of the estimation deduced from a spectrally integrated measurement and also to the imprecision of the efficiency curve deduced

from the manufacturer datasheets and used to correct the raw spectrum.

Having inferred the effective temperature of the electron subsystem, we extract the contribution of the prefactor  $\rho(\nu)$  by normalizing the experimental spectrum by  $h\nu e^{-h\nu/k_B T_e}$ . The spectral landscape of the prefactor is shown in the inset of Fig. 4(a). Weak resonances can be seen when  $\rho(\nu) > 1$  at 1.42 and 1.66 eV, which are reminiscent of the underlying geometry. Because the device is reconfiguring itself at every voltage pulse (volatile switching), the spectral position and strength of the resonances are likely to vary from pulse to pulse. This is illustrated by the spectrum of the third event displayed in Fig. 4(b). This event was the weakest of the three with no marked resonances. The spectrum is displayed in semilogarithmic scale to visualize the exponential behavior expected from Eq. (2) and clearly confirms the overbias nature of the emitted photons. The fit gives an effective electronic temperature at 2300 K, a slightly higher value compared to the second event despite a lower emitted photon rate. This may be understood from the fact that no resonances are present to increase the radiation efficiency of the thermal emission. Unfortunately, the first event was not captured by the spectrometer because of a synchronization problem with the voltage pulses.

As a point of discussion, we note that in a 2020 paper, Fung and Venkataraman questioned this hot-electron picture on the basis of data obtained by scanning tunneling

microscopy experiment. They proposed an alternative emission mechanism involving multielectron interactions [42] and were able to reproduce their nonlinear  $(\alpha IV_b)^{-0.5}$  dependence by considering a third-order process. Nevertheless, coherent interactions between carriers are not a major contribution in our measurement because (i) our data obtained with a greater range of electrical power reasonably collapse on a linear relationship with  $(\alpha IV_b)^{-0.5}$  in log scale, and (ii) of the absence of spectral kink at  $eV_b$ . The probable difference is linked to the system geometry. A planar memristive device and its associated thermalization processes significantly differ from STM-based measurements. We note however that a crossover between coherent multielectron overbias emission and hot-carrier radiation has been recently observed for in-plane Al electromigrated gaps placed in a cryostat where hot-electron radiation was shown to be prevalent with noble metal plasmonic systems [49]. In our Ag memristive junction operated at ambient conditions, the density of optical states is dominated by a complex surface plasmon spectral landscape, favoring thus a hot-electron overbias emission regime. This is readily shown from the local density of modes extracted in the inset of Fig. 4(a) featuring a compound dispersion for this switching pulse. Additionally, because of the very small

interaction area, energy dissipation is mainly guided by electrons interacting with the surface rather than electron-phonon interactions [47] and we were not able to observe co-existing emission regimes.

These series of measurement and dependencies were observed on a set of data acquired during a second run obtained with the same device and under the same biasing conditions. This is shown in Fig. 5, which is complementing and confirming the trends discussed in Figs. 2 and 3. The time traces of the current [Fig. 5(a)] and the photon count rate [Fig. 5(b)] display a strongly fluctuating behavior between all switching pulses (voltage signal not shown). Again, periods of more stable LRS such as  $t < 10$  s,  $60 \text{ s} < t < 70$  s, or  $80 \text{ s} < t < 105$  s do not provide any appreciable photon counts. In contrast, current spikes associated with a reorganization of the filamentary path are generally responsible for an overbias activity. Out of the many spikes present, we select an event where  $G \sim 0.2G_0$  labeled with an arrow in Fig. 5(b). We then conduct the same analysis as in Fig. 3 to confront the data with the thermal radiation model. The results are plotted in Fig. 5(c) in a semilogarithmic plot and unambiguously confirms the previous findings. The linear dependence to  $\sqrt{IV_b}$  gives a slope  $|\beta| = 20 \times 10^{-3} \text{ W}^{1/2}$ . We then infer  $\beta$  for all the

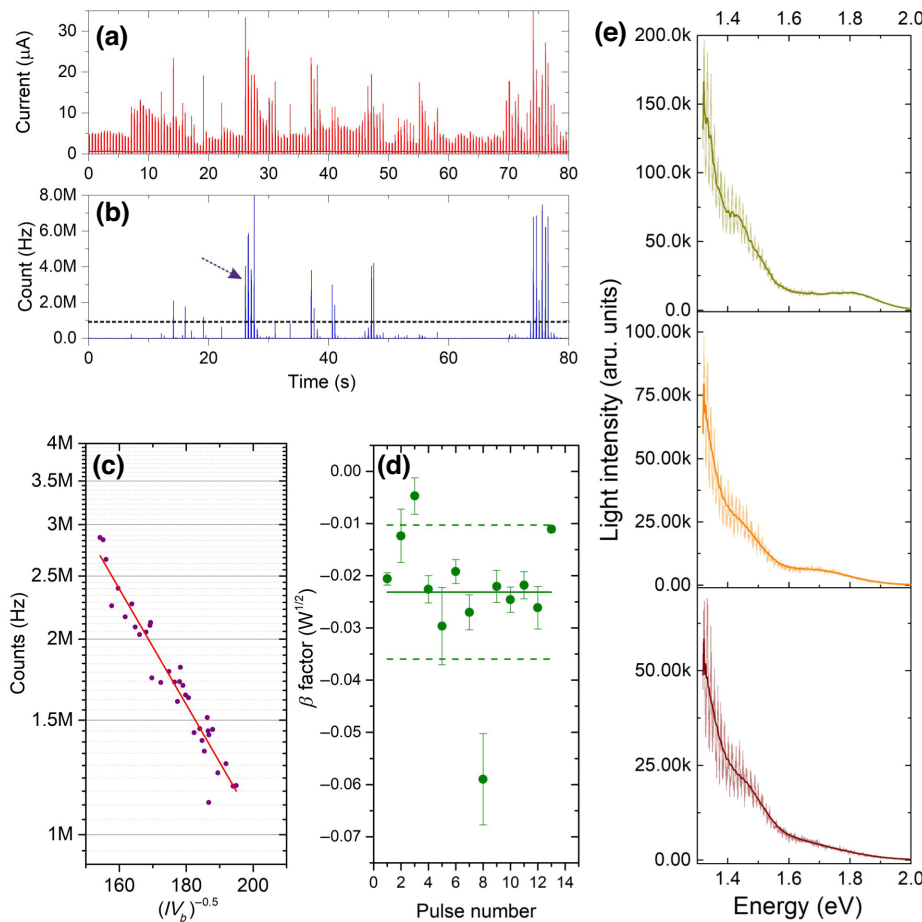


FIG. 5. (a),(b) Time traces of the measured current and the detected count rate during a second run with the same pulse sequence (no shown). (c) Logarithmic plots of the spectrally integrated count rate as a function of  $1/\sqrt{IV_b}$  for the event labeled by an arrow in (b). The slope of the linear fit (red line) provides  $\beta$  for this event. (d) Values of  $\beta$  estimated from events brighter than 1 MHz [dotted horizontal line in (b)]. The solid line is the mean value and the dotted lines are  $1\sigma$  deviation. (e) Series of three spectra acquired during the three consecutive pulses starting at that arrow in (b). Thick solid lines are adjacent averaging of the raw data.



events with a count rate greater than 1 MHz [dashed horizontal line in Fig. 5(b)]. The results are plotted in Fig. 5(d). A couple of pulses are outside the standard deviation  $\sigma$ , but most of the  $\beta$  are near the mean value (solid line). This suggests that the device intermittently recovers the condition to create hot electronic subsystems during the sequence despite a stochastic atomic reorganization of the current channels. To complement the discussion, we also show the emitted spectra associated to three consecutive photon spikes occurring after the arrow [Fig. 5(b)]. These are shown in Fig. 5(e) and correspond, from top to bottom, to pulses at  $t = 26.55$  s,  $t = 27.05$  s, and  $t = 27.55$  s. Despite a change in amplitude, the spectra are generally sharing the same thermal trend discussed in Fig. 4(a). The shoulders structuring the three spectra have different strengths and energy positions; this is consistent with a stochastic

reshaping of the local plasmonic environment during each of the pulses already discussed above.

## V. FROM OVERBIAS TO INELASTIC ELECTRON TUNNELING EMISSION REGIME

At some point in the electro-optical evolution of the device with a constant voltage pulse, the emission of light eventually vanished because the filament gradually became more and more stable and reached a nonvolatile switching behavior. We therefore increased the amplitude of the pulses to recover photon emission for subsequent sequences and recorded the time traces of the different signals. An example is shown in Fig. 6(a) for  $V_b = 1.6$  V pulses with a period of 400 ms and a duration of 200 ms. The current shows a somewhat stable level across this

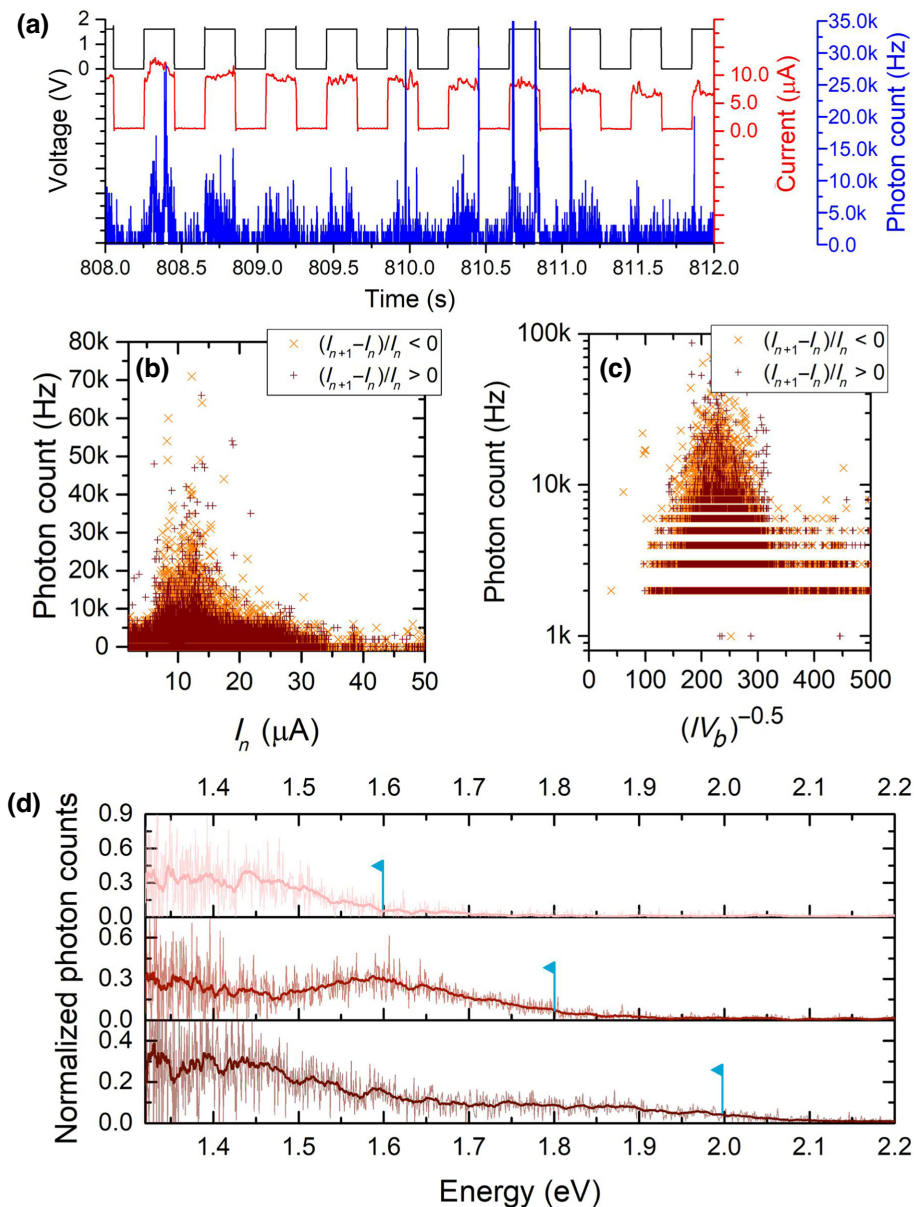


FIG. 6. (a) Extract of a cycling sequence showing the photon counts and the current for a pulse train of 1.6 V, 400-ms period, and 200-ms duration. (b) Photon counts versus the relative change of the current. Any correlative features are absent compared to Fig. 3(a). (c) Logarithmic plot of the count rate as a function of the inverse square root of the dissipated power extracted from the entire sequence for both signs of the current variations. The linear dependence expected from Eq. (2) is no longer found. (d) Series of normalized electroluminescent spectra emitted by the memristive gap upon application of different pulse amplitudes  $V_b = 1.6$  V (top),  $V_b = 1.8$  V (middle), and  $V_b = 2$  V (bottom). The vertical flags are marking the quantum limit given by  $h\nu = eV_b$ .

time extract and rise concomitantly to the front edge of the voltage pulse. The device operates in a nonvolatile configuration indicating that the conduction path holds its characteristics in the lag time between pulses. Despite a relative stability of the current, a small number of photons are detected at every pulse. This departs from overbias emission where a volatile resistive switching from HRS to LRS is observed. Clearly a different light-emission mechanism is now ruling the dynamics of the device. As shown in Fig. 6(b), the correlative dependencies (branches) with  $\Delta I/I$  previously revealed in Fig. 3(a) are no longer observed, regardless of the sign of the current variation. We confirm this by confronting the data to Eq. (2). The linear dependence associated with overbias emission and the spontaneous decay of nonequilibrium electrons [see Fig. 3(b)] is not found anymore in Fig. 6(c) despite comparable dissipated electrical powers. The most likely emission process that explains the data is inelastic electron tunneling whereby an electron injected in the gap has a small probability to lose its energy by exciting optical modes [51]. The measured efficiency is here even weaker than the overbias regime with a QE of the order of  $10^{-10}$  photon per electron and is far lower than plasmon-optimized devices reported in the literature [23,52]. For IET, the high energy side of the emitted spectrum is no longer limited by the electron effective temperature but by the quantum limit  $h\nu \leq eV_b$ . Figure 6(d) shows a series of spectra emitted by the device for three different pulse amplitudes. The spectra are integrated during a single period and leads to the noisy signal since the photon rate here is comparatively weaker than in Fig. 5(b). The vertical flags mark the kinetic energy of the electrons as supplied by the operating voltage. As expected, photons are no longer emitted in the overbias regime and the highest photon energy is now bounded by  $eV_b$ . This undoubtedly confirms a change of the emission process favoring inelastic electron tunneling. Note that the spectra feature shoulders that bear some similarities with the overbias spectra displayed in Fig. 5(e). Despite a different emission regime, the spectra reflect the underlying electromagnetic environment. Our data suggests that the crossover between IET and overbias is intimately linked to the dynamic reorganization of the conduction path during the OFF state. If the conduction path significantly relaxes to reach a volatile state, overbias emission can be observed providing that the electrical power injected in the system is sufficient to bring the electron temperature to emit in the spectral detection window.

## VI. CONCLUSION

We report that resistive switching in filament-type memristive Ag/SiO<sub>2</sub>/Ag junction may be accompanied by light emission. We show in our experiments that two mechanisms are at play depending on the nature and the dynamics of the switching. When toggling from a high resistive state

to a volatile low resistive state, we observe photons emitted in the so-called overbias regime. In this particular emission process, photons released by the device are emitted by the radiative decay of out-of-equilibrium electrons brought at elevated temperature ( $>2000$  K). This is made possible by operating the memristor in a transient mode with large current ( $>10$   $\mu$ A) and relatively low pulse voltages (100 ms, approximately 1 V) triggering a resistive switching near  $G_0$  conductance. The overbias spectrum is well described by a blackbody thermal radiation model that combines the Planck term with a local density of states reflecting the underlying surface plasmon landscape and material properties. These dependencies suggest that structuring the local electromagnetic environment of the memristor near the resistive switching region allows to engineer the emission spectrum and may help to increase the efficiency of the process. We also stress that the stability of the low resistive state is strongly reduced when hot carriers are generated.

Overbias emission does not occur systematically for every switching voltage pulse. This underpins the drastic influence of the diffusion dynamics of the Ag atoms reconfiguring the current pathway within the dielectric medium. For nonvolatile cycles, we observe a crossover in the emission mechanism with signature of inelastic electron tunneling events that are no longer associated with a stochastic transient evolution of the current. Instead, systematic light emission is detected at each voltage pulse, albeit with a lower photon rate. Controlling and stabilizing the switching conditions will be essential to use the released photons in the next generation of optimized photonic memristors. Thus, this alternative family of atomic size devices can act as integrated sources of broadband radiation with temporal bandwidth only limited by the electron-phonon energy exchange time. This mixed photonic and electrical responses are confirming the ability of memristive gaps to not only emulate the biological electrical activity of neurons, but also to mimic the generation of biophotons [53,54].

## ACKNOWLEDGMENTS

This work has been partially funded by the French Agence Nationale de la Recherche (ANR-20-CE24-0001 DALHAI and ISITE-BFC ANR-15-IDEX-0003), the EIPHI Graduate School (ANR-17-EURE-0002), and the European Union through the PO FEDER-FSE Bourgogne 2014/2020 programs. E.T.H. acknowledges support of the Werner Siemens-Stiftung (WSS). Device characterization was performed at the technological platforms SMART-LIGHT and ARCEN Carnot with the support of the French Agence Nationale de la Recherche under program Investment for the Future (ANR-21-ESRE-0040), the Région de Bourgogne Franche-Comté, the CNRS and the French Renatech+ network.

- [1] H. Xu, E. Bjerneld, M. Käll, and L. Börjesson, Spectroscopy of Single Hemoglobin Molecules by Surface Enhanced Raman Scattering, *Phys. Rev. Lett.* **83**, 4357 (1999).
- [2] J. J. Baumberg, J. Aizpurua, M. H. Mikkelsen, and D. R. Smith, Extreme nanophotonics from ultrathin metallic gaps, *Nat. Mater.* **18**, 668 (2019).
- [3] G. C. Solomon, C. Herrmann, T. Hansen, V. Mujica, and M. A. Ratner, Exploring local currents in molecular junctions, *Nat. Chem.* **2**, 223 (2010).
- [4] D. R. Ward, N. J. Halas, J. W. Ciszek, J. M. Tour, Y. Wu, P. Nordlander, and D. Natelson, Simultaneous measurements of electronic conduction and Raman response in molecular junctions, *Nano Lett.* **8**, 919 (2008).
- [5] J. J. Baumberg, Picocavities: A primer, *Nano Lett.* **22**, 5859 (2022).
- [6] W. Chen, P. Roelli, H. Hu, S. Verlekar, S. P. Amirtharaj, A. I. Barreda, T. J. Kippenberg, M. Kovylyna, E. Verhagen, A. Martinez, and C. Galland, Continuous-wave frequency upconversion with a molecular optomechanical nanocavity, *Science* **374**, 1264 (2021).
- [7] R. Esteban, A. G. Borisov, P. Nordlander, and J. Aizpurua, Bridging quantum and classical plasmonics with a quantum-corrected model, *Nat. Commun.* **3**, 825 (2012).
- [8] M. S. Tame, K. R. McEnery, S. K. Özdemir, J. Lee, S. A. Maier, and M. S. Kim, Quantum plasmonics, *Nat. Phys.* **9**, 329 (2013).
- [9] Y. Pang and R. Gordon, Optical trapping of a single protein, *Nano Lett.* **12**, 402 (2012).
- [10] J. Berthelot, S. S. Aćimović, M. L. Juan, M. P. Kreuzer, J. Renger, and R. Quidant, Three-dimensional manipulation with scanning near-field optical nanotweezers, *Nat. Nanotech.* **9**, 295 (2014).
- [11] Y. Li, Z. Wang, R. Midya, Q. Xia, and J. J. Yang, Review of memristor devices in neuromorphic computing: materials sciences and device challenges, *J. Phys. D: Appl. Phys.* **51**, 503002 (2018).
- [12] L. Ye, Z. Gao, J. Fu, W. Ren, C. Yang, J. Wen, X. Wan, Q. Ren, S. Gu, X. Liu, X. Lian, and L. Wang, Overview of memristor-based neural network design and applications, *Front. Phys.* **10**, 839243 (2022).
- [13] D. Ielmini and S. Ambrogio, in *Advances in Non-Volatile Memory and Storage Technology*, edited by B. Magyari-Köpe and Y. Nishi (Woodhead Publishing, 2019), 2nd ed., p. 603.
- [14] T. Tsuruoka, K. Terabe, T. Hasegawa, and M. Aono, Forming and switching mechanisms of a cation-migration-based oxide resistive memory, *Nanotechnology* **21**, 425205 (2010).
- [15] C. Funck and S. Menzel, Comprehensive model of electron conduction in oxide-based memristive devices, *ACS Appl. Electron. Mater.* **3**, 3674 (2021).
- [16] J. Yao, L. Zhong, D. Natelson, and J. M. Tour, In situ imaging of the conducting filament in a silicon oxide resistive switch, *Sci. Rep.* **2**, 242 (2012).
- [17] Y. Yang, P. Gao, L. Li, X. Pan, S. Tappertzhofen, S. Choi, R. Waser, I. Valov, and W. D. Lu, Electrochemical dynamics of nanoscale metallic inclusions in dielectrics, *Nat. Commun.* **5**, 4232 (2014).
- [18] C.-W. Chang, W.-C. Tan, M.-L. Lu, T.-C. Pan, Y.-J. Yang, and Y.-F. Chen, Electrically and optically readable light emitting memories, *Sci. Rep.* **4**, 5121 (2014).
- [19] D. T. Schoen, A. L. Holsteen, and M. L. Brongersma, Probing the electrical switching of a memristive optical antenna by stem eels, *Nat. Commun.* **7**, 12162 (2016).
- [20] A. Emboras, J. Niegemann, P. Ma, C. Haffner, A. Pedersen, M. Luisier, C. Hafner, T. Schimmel, and J. Leuthold, Atomic scale plasmonic switch, *Nano Lett.* **16**, 709 (2016).
- [21] U. Koch, C. Hoessbacher, A. Emboras, and J. Leuthold, Optical memristive switches, *J. Electroceram.* **39**, 239 (2017).
- [22] J. Tang, H. Hu, X. He, Y. Xu, Y. Zhang, Z. Guan, S. Zhang, and H. Xu, Switchable electrically driven optical antenna based on ultrathin amorphous silica, *Adv. Opt. Mat.* **9**, 2100191 (2021).
- [23] J. Kern, R. Kullock, J. C. Prangma, M. Emmerling, M. Kamp, and B. Hecht, Electrically-driven optical antennas, *Nat. Photonics* **9**, 582 (2015).
- [24] M. Parzefall and L. Novotny, Optical antennas driven by quantum tunneling: A key issues review, *Rep. Progr. Phys.* **82**, 112401 (2019).
- [25] B. Cheng, T. Zellweger, K. Malchow, X. Zhang, M. Lewerenz, E. Passerini, J. Aeschlimann, U. Koch, M. Luisier, A. Emboras, A. Bouhelier, and J. Leuthold, Atomic scale memristive photon source, *Light: Sci. Appl.* **11**, 78 (2022).
- [26] P. Tomchuk and R. Fedorovich, Emission of hot electrons from thin metal films, *Sov. Phys. Sol. Stat.* **276**, 276 (1966).
- [27] M. Buret, A. V. Uskov, J. Dellinger, N. Cazier, M.-M. Mennemanteuil, J. Berthelot, I. V. Smetanin, I. E. Protsenko, G. Colas-des-Francis, and A. Bouhelier, Spontaneous hot-electron light emission from electron-fed optical antennas, *Nano Lett.* **15**, 5811 (2015).
- [28] L. Cui, Y. Zhu, M. Abbasi, A. Ahmadivand, B. Gerislioglu, P. Nordlander, and D. Natelson, Electrically driven hot-carrier generation and above-threshold light emission in plasmonic tunnel junctions, *Nano Lett.* **20**, 6067 (2020).
- [29] T. Malinowski, H. R. Klein, M. Iazykov, and P. Dumas, Infrared light emission from nano hot electron gas created in atomic point contacts, *Europhys. Lett.* **114**, 57002 (2016).
- [30] A. Downes, P. Dumas, and M. E. Welland, Measurement of high electron temperature in single atom metal point contacts by light emission, *Appl. Phys. Lett.* **81**, 1252 (2002).
- [31] P.-J. Peters, F. Xu, K. Kaasbjerg, G. Rastelli, W. Belzig, and R. Berndt, Quantum Coherent Multielectron Processes in an Atomic Scale Contact, *Phys. Rev. Lett.* **119**, 066803 (2017).
- [32] Z. Wang, S. Joshi, S. E. Savel'ev, H. Jiang, R. Midya, P. Lin, M. Hu, N. Ge, J. P. Strachan, Z. Li, Q. Wu, M. Barnell, G.-L. Li, H. L. Xin, R. S. Williams, Q. Xia, and J. J. Yang, Memristors with diffusive dynamics as synaptic emulators for neuromorphic computing, *Nat. Mater.* **16**, 101 (2017).
- [33] K. Patel, J. Cottom, M. Bosman, A. Kenyon, and A. Shluger, An oxygen vacancy mediated Ag reduction and nucleation mechanism in SiO<sub>2</sub> RRAM devices, *Microelectron. Reliab.* **98**, 144 (2019).

- [34] B. Cheng, A. Emboras, Y. Salamin, F. Ducry, P. Ma, Y. Fedoryshyn, S. Andermatt, M. Luisier, and J. Leuthold, Ultra compact electrochemical metallization cells offering reproducible atomic scale memristive switching, *Commun. Phys.* **2**, 28 (2019).
- [35] J. Michaelis, C. Hettich, J. Mlynek, and V. Sandoghdar, Optical microscopy using a single molecule light source, *Nature* **405**, 325 (2000).
- [36] M. Lübben, S. Menzel, S. G. Park, M. Yang, R. Waser, and I. Valov, Set kinetics of electrochemical metallization cells: influence of counter-electrodes in SiO<sub>2</sub>/Ag based systems, *Nanotechnology* **28**, 135205 (2017).
- [37] R. Pechou, R. Coratger, F. Ajustron, and J. Beauvillain, Cutoff anomalies in light emitted from tunneling junction of a scanning tunneling microscope in air, *Appl. Phys. Lett.* **72**, 671 (1998).
- [38] G. Schull, N. Néel, P. Johansson, and R. Berndt, Electron-Plasmon and Electron-Electron Interactions at a Single Atom Contact, *Phys. Rev. Lett.* **102**, 057401 (2009).
- [39] N. L. Schneider, P. Johansson, and R. Berndt, Hot electron cascades in the scanning tunneling microscope, *Phys. Rev. B* **87**, 045409 (2013).
- [40] F. Xu, C. Holmqvist, and W. Belzig, Overbias Light Emission due to High-Order Quantum Noise in a Tunnel Junction, *Phys. Rev. Lett.* **113**, 066801 (2014).
- [41] K. Kaasbjerg and A. Nitzan, Theory of Light Emission from Quantum Noise in Plasmonic Contacts: Above-Threshold Emission from Higher-Order Electron-Plasmon Scattering, *Phys. Rev. Lett.* **114**, 126803 (2015).
- [42] E.-D. Fung and L. Venkataraman, Too cool for blackbody radiation: Overbias photon emission in ambient STM due to multielectron processes, *Nano Lett.* **20**, 8912 (2020).
- [43] Y. Zhu, L. Cui, and D. Natelson, Hot-carrier enhanced light emission: The origin of above-threshold photons from electrically driven plasmonic tunnel junctions, *J. Appl. Phys.* **128**, 233105 (2020).
- [44] K. L. Chopra, L. C. Bobb, and M. H. Francombe, Electrical resistivity of thin single crystal gold films, *J. Appl. Phys.* **34**, 1699 (1963).
- [45] S. Sze, J. Moll, and T. Sugano, Range-energy relation of hot electrons in gold, *Solid State Electron.* **7**, 509 (1964).
- [46] R. Fedorovich, A. Naumovets, and P. Tomchuk, Electron and light emission from island metal films and generation of hot electrons in nanoparticles, *Phys. Rep.* **328**, 73 (2000).
- [47] M. Buret, I. V. Smetanin, A. V. Uskov, G. Colas des Francs, and A. Bouhelier, Effect of quantized conductivity on the anomalous photon emission radiated from atomic-size point contacts, *Nanophotonics* **9**, 413 (2020).
- [48] G. Ghisellini, *Radiative Processes in High Energy Astrophysics* (Springer, Heidelberg, 2013).
- [49] Y. Zhu, L. Cui, M. Abbasi, and D. Natelson, Tuning light emission crossovers in atomic-scale aluminum plasmonic tunnel junctions, *Nano Lett.* **22**, 8068 (2022).
- [50] J. B. Herzog, M. W. Knight, Y. Li, K. M. Evans, N. J. Halas, and D. Natelson, Dark plasmons in hot spot generation and polarization in interelectrode nanoscale junctions, *Nano Lett.* **13**, 1359 (2013).
- [51] M. Parzefall and L. Novotny, Light at the end of the tunnel, *ACS Photonics* **5**, 4195 (2018).
- [52] H. Qian, S.-W. Hsu, K. Gurunatha, C. T. Riley, J. Zhao, D. Lu, A. R. Tao, and Z. Liu, Efficient light generation from enhanced inelastic electron tunnelling, *Nat. Photonics* **12**, 485 (2018).
- [53] C. Moro, A. Liebert, C. Hamilton, N. Pasqual, G. Jeffrey, J. Stone, and J. Mitrofanis, The code of light: Do neurons generate light to communicate and repair?, *Neural Regen. Res.* **17**, 1251 (2022).
- [54] P. Zarkeshian, T. Kergan, R. Ghobadi, W. Nicola, and C. Simon, Photons guided by axons may enable backpropagation-based learning in the brain, *Sci. Rep.* **12**, 20720 (2022).